International Journal of Technology 13(4) 764-773 (2022)
Received August 2021 / Revised February 2022 / Accepted May 2022

International Journal of Technology

http://ijtech.eng.ui.ac.id

Computational Modeling of Thermo-Metallurgical Behavior During the TIG Welding Process

Karim Agrebi[1*], Asma Belhadj[1], Jamel Bessrour[1], Mahmoud Bouhafs[1]

[1]*Laboratory of Applied Mechanics and Engineering, University of Tunis EL Manar, National Engineering School of Tunis, BP 37, Le Belvédère, 1002, Tunisia*

Abstract. Welding is widely used in the aerospace, naval and automotive industries. Since high temperatures are involved in this process, solid state metallurgical changes are expected. These metallurgical changes can induce deformations and residual stresses in welded parts. The objective of this work is to develop a finite element calculation code, under the MATLAB environment, to predict the evolution of the various metallurgical transformations during TIG welding of C50 steel plates. In the proposed calculation procedure, we used Leblond's equation and Waeckel's model to characterize the metallurgical transformations during respectively heating and cooling stage. We also taken into account the effect of austenitic grain size on metallurgical transformations evolution. Thermal properties are introduced according temperature and phase proportions present during welding operation. Simulation results show that the metallurgical structure in the heat affected zone (HAZ) is largely related to welding thermal power and the plate preheating temperature. We compared simulation results to experimental measurements and the efficiency of the developed computational code was confirmed.

Keywords: Coupled Thermo-Metallurgical modeling; Experimental study; Finite element simulation; TIG welding

1. Introduction

Welding is a necessary industrial process that persistently needs to be developed. For this aim, numerical prediction of welded parts behaviors is an alternative, which avoids the cost of the experimental analysis. During welding processes, located and moving heat source generates, after cooling, important residual stresses in welded parts. These stresses are the results of the heterogeneity of deformation due to changes in temperature and in metallurgical transformation in the different parts of the weld. This work concerns the modeling and the finite element simulation of these microstructural transformations during the welding operation of a plate in C50 steel.

Several authors have implemented thermomechanical and metallurgical models in numerical calculation codes to study the generation of residual stresses due to metallurgical transformations during welding. Ronda et al. (2000) presented the results of a numerical simulation of welding problem based on electromagnetic, thermal, mechanical and metallurgical modelling. Results of this numerical simulation are shown for two simple welding benchmark problems formulated for two thick plates. Using ABAQUS, Deng (2009)

*Corresponding author's email: agrebikarim@ymail.com, Tel.: +216 92 819 718 Fax.: +216 71 874 700
doi: 10.14716/ijtech.v13i4.5083

developed a thermo-metallurgical-mechanical computational model to predict the residual stresses in 2.25Cr - 1Mo steel pipes butt-welded in several passes. The simulation results show that yield strength change affect welding residual stresses in 2.25 Cr–1Mo steel pipes. Using SYSWELD software, Li et al. (2017) developed a thermo-metallurgical-mechanical finite element model to predict welding residual stresses in P92 steel joints. The experimental measurements verified the effectiveness of the developed computational approach. Heinze et al. (2012) studied the influence of austenitic grain size on the residual stresses distribution after steel welding. Numerical results have shown the impact of austenite grain size on the residual stress development. Xia et al. (2018) propose a finite element simulation procedure to model the thermo-metallurgical coupling phenomena of welding using the ABAQUS software. The proposed coupled analysis simulation model is confirmed by the excellent agreement between the simulated and experimental results.

Sun et al. (2019) performed a series of numerical simulations on the SIMUFACT software, to examine the variability of welding residual stresses for different materials. The result shows that the mixed hardening model provides the most accurate prediction of residual stresses. Zain-Ul-Abdein et al. (2011) developed a comparative study between two finite element models established on ABAQUS and SYSWELD. They studied the effect of metallurgical transformations on residual stresses and distortions induced by laser beam welding in a T-joint configuration. The results show that considering metallurgical changes has a negligible effect on the predicted distortions but not on the residual stresses distribution.

Other researchers have developed numerical computer codes for the welding process simulation. Hamide et al. (2008) contributed to developing an adaptive mesh module for the TRANSWELD software to simulate the thermo-metallurgical coupled behavior of a fusion line produced on a steel plate by a TIG welding station. Hendili et al. (2013) contributed to developing a metallurgical behavior module established in CODE ASTER. They used Leblond's equation to describe the formation of the austenitic phase during heating stage and the Waeckel's model to describe the decomposition of the austenitic phase during the cooling stage.

Several other studies present numerical and experimental characterization of welded assemblies. Baskoro et al. (2017) investigated the influence of micro-resistance spot welding parameters on the mechanical properties and failure of an aluminum alloy 1100 nugget. Baskoro et al. (2011) propose a study comparing particle swarm optimization with a genetic algorithm for molten pool detection in fixed aluminum pipe welding. Rupajati et al. (2021) investigate the characteristics of the lap shear force and microstructure of micro friction stir spot welding joints.

Our numerical tool developed under MATLAB environment is a new personalized numerical calculation code, simple and flexible. With this tool, we have tried to solve some of the difficulties that exist in using commercial codes to simulate the welding process. For example, the study of metallurgical behavior or the heat source moving simulation during welding cannot be done directly on some commercial software. Indeed, to predict the behavior of parts during welding on ABAQUS for example, we need to program the metallurgical behavior laws on FORTRAN. In our case, the metallurgical changes and source moving peculiarities of the welding processes study are integrated into our numerical calculation code. The computer code will be used to perform thermomechanical and metallurgical calculations during the TIG welding operation. This article is about the development of the thermo-metallurgical model.

2. Method

2.1. Hypotheses

In the present work, thermal calculations do not consider convective motion in the weld pool as well as the heat exchange due to the metallurgical transformations latent heat. Heat transfer in the molten bath is assumed to be conductive.

2.2. Thermal analysis

During welding, the plate receives a mobile heat flow located on the irradiated zone $\partial\Omega_{\mathrm{TIG}}$. The temperature increases and locally reaches the melting point. A liquid metal pool is formed. The heat is propagated by conduction in the unit volume Ω and by convection and radiation on the plate surface $\partial\Omega$. Figure 1 illustrates heat exchanges during the TIG welding process.

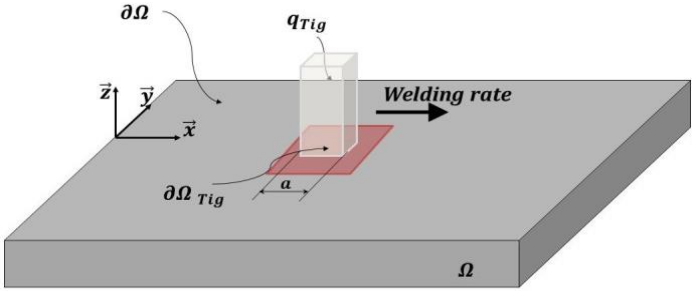

Figure 1 Heat transfer during welding

The thermal problem is governed by the energy balance equation using enthalpy formulation to take into account the phase changes. This equation controls the temperature and the solidification evolution and it can be stated as a function of the enthalpy state variable per unit of volume $H(\mathrm{T})$ (Equation 1):

$$\nabla\left(\lambda(T)\ \vec{\nabla}T\right) = \rho(T).\frac{dH}{dt}\ \forall\ M \in \Omega \tag{1}$$

T is the temperature, $\lambda(T)$ is the material thermal conductivity, $\rho(T)$ is the material density and $H(T)$ is the specific enthalpy given by equation 2 (Agrebi et al., 2019):

$$H(T) = \int_{T_r}^{T} C_p(\tau)\,.\,d\tau + g_l.L_f \tag{2}$$

$C_p(T)$ is the specific heat, T_r is the room temperature, L_f is the specific fusion latent heat and g_l is the liquid ratio. The thermo-physical parameters are calculated taking into account the structural transformations by a linear mixing law given by equations 3, 4 and 5.

$$\lambda(T) = \sum_X Z_X \lambda_X(T) \tag{3}$$
$$\rho(T) = \sum_X Z_X \rho_X(T) \tag{4}$$
$$C_p(T) = \sum_X Z_X C_{p_X}(T) \tag{5}$$

X designates one of the following metallurgical phases: austenite, bainite, ferrite, perlite and martensite, $\lambda_X(T)$ is the thermal conductivity of phase X, $\rho_X(T)$ is the density of phase X, $C_{p_X}(T)$ is the specific heat of phase X and Z_X is the ratio of phase X.

The plate is welded in the open air, so convection and radiation heat transfer are applied on $\partial\Omega$ (Equation 6-7).

$$-k.\vec{\nabla}T = h.(T - T_r)\vec{n}\ on\ \partial\Omega \tag{6}$$
$$-k.\vec{\nabla}T = \varepsilon.\sigma.\left(T^4 - {T_r}^4\right)\vec{n}\ on\ \partial\Omega \tag{7}$$

h is exchange coefficient by convection, ε is the radiation emissivity and σ is Stephan Boltzmann's constant.

A heat flow is imposed on the area irradiated by the electric arc (Equation 8).

$$-k.\vec{\nabla}T = q_{tig}.\vec{n}\ on\ \partial\Omega_{Tig} \tag{8}$$

The heat source is modeled by a surface uniform heat distribution on a square of side a. The heat flux expression is given by the equation 9:

$$q_{Tig} = \frac{\eta UI}{a^2} \quad (9)$$

U is the welding voltage, I is the welding current intensity and η is the arc station performance.

For considerations of symmetry, the calculation is made on half of the plate. We impose a zero heat flow on the symmetry plane $\partial\Omega_{Sym}$ (Equation 10)

$$-k.\vec{\nabla}T = \vec{0}\ on\ \partial\Omega_{Sym} \quad (10)$$

The initial temperature of the plate is 20 ° C (Equation 11)

$$T = 20°C\ at\ t = 0\ s\ \forall\ M \in \Omega \quad (11)$$

2.3. Metallurgical Analysis

To calculate the evolution of the metallurgical transformations during and after the welding operation we use:

- The Leblond's equation (Equation 12-13) during the heating phase
- The waeckel's model (Equation 14) for transformations by diffusion during the cooling phase
- The Koistinen and Marburger equation (Equation 15) for the martensitic transformation during the cooling phase

$$\dot{Z} = \left(Z_{eq}(T) - Z(T)\right)/\tau(T) \quad (12)$$

$$\tau(T) = \alpha.(T - A_{e1})^{-\beta} \quad (13)$$

Z(T) is the austenite ratio at temperature T, $Z_{eq}(T)$ is the austenite ratio formed under equilibrium conditions at temperature T, α and β are model parameters and A_{e1} the austenite formation beginning temperature in equilibrium condition.

$$\dot{Z} = f\left(t, T, \dot{T}, Z; d\right) \quad (14)$$

$\dot{T}$ is the temperature rate, d is the austenitic diameter.

$$\dot{Z} = Z_{max}.[1 - \exp(-0.011x(Ms - T)] \quad (15)$$

Z_{max} is the maximum austenite ratio and Ms is the beginning temperature of the martensite transformation.

The austenitic grain size, during the heating stage, can be computed by using Gray and Higgins's equation (Equation 16-17-18):

$$\dot{d} = (1/k).\left((1/d) - (1/d_{lim})\right) - \left(\dot{Z}/Z\right).d \quad (16)$$

$$k = k_0.exp(Q/R.T) \quad (17)$$

$$d_{lim} = d_{10}.exp(-W/R.T) \quad (18)$$

R is the ideal gas constant(8.32 J/mol. K), $k_0$is the reverse of viscosity of the molten metal ($s/\mu m^2$), Q is material parameter(J/mol) (homogeneous to an activation energy), W is material parameter (J/mol) (homogeneous to an activation energy) and d_{10} is the limit value for the austenitic grain diameter (μm).

We assume that the effect of the austenitic grain size on the metallurgical changes during the cooling stage is manifested by a change in the cooling kinetics according to the equation 19 (Hendili et al., 2013):

$$\dot{T} = \dot{T}_{th}.exp\left(c.(d - d_{ref})\right) \quad (19)$$

$\dot{T}_{th}$ is the cooling rate from thermal calculation, $\dot{T}$ is the cooling rate used in the metallurgical calculation to take into account the effect of the austenitic grain size, d_{ref} is CCT diagram reference diameter of C50 steel. It has taken equal to 15 µm. We identify the coefficient c by the reverse method from the hardness measurements. It has taken similar to 0.003 μm^{-1}.

A mixing law computes the hardness according to the equation 20 (Hendili et al., 2013):

$$H_v = \sum_X Z_X V_X \quad (20)$$

X designates one of the following metallurgical phases: bainite, ferrite, perlite and martensite; V_X is the hardness of phase X; H_v is the hardness on a point of the plate.

The hardness value of the different metallurgical phases is approximated from the CCT diagram of C50 steel (Table 1).

Table 1 Hardness value of metallurgical phases.

Phase	Ferrite	Perlite	Bainite	Martensite
Hardness(hv)	4	313	313	700

3. Material Properties

The plate is made of C50 steel, table 2 gives the chemical composition of which.

Table 2 Chemical composition of C50 steel by percentage weight

C	Si	Mn	S	Cr+Ni+Mo
0.45-0.50	≤ 0.4	0,5-0,8	0,015-0,035	≤ 0,63

The specific capacity heat, thermal conductivity and density of the metallurgical phases are taken from Heinze et al. (2012). We identify the metallurgical model parameters of the heating phase from the austenization thermal transformation diagram of C50 steel (Table 3).

Table 3 Physical parameters of the metallurgical model for heating phase

$\boldsymbol{\alpha}$	$3.\ 10^{-7}$
$\boldsymbol{\beta}$	3.8
$\mathbf{k_0}$	10^{-14} s/ µm²
Q	$3.2x10^5$ J/mol
W	1000 J/mol
$\mathbf{d_{10}}$	300 µm

4. Numerical Formulation

4.1. Thermal Problem

A non-uniform fixed mesh in three dimensions is used. A hexahedral mesh forms the mesh with eight nodes. We made the calculation on half of the plate for symmetry considerations. 29898 nodes and 24000 elements form the mesh. The time step is equal to 0.5s (Figure 2). More detail for the numerical formulation of the thermal problem is given in Agrebi et al. (2019).

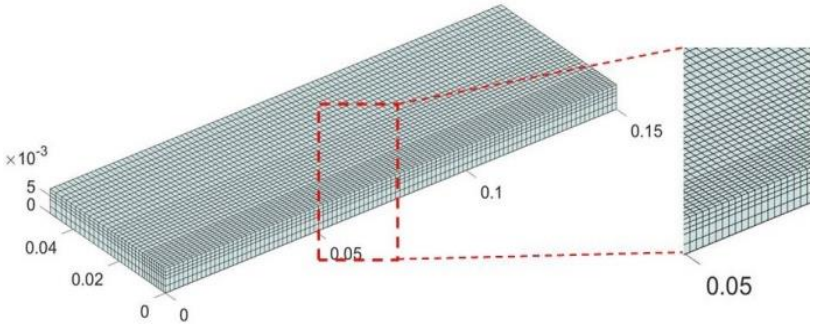

Figure 2 Finite element model

4.2. Metallurgical problem

In this part, we present the numerical formulation to solve the metallurgical model. The numerical resolution of the energy balance equation (Equation 1), provides the temperature evolution for each node of the mesh and at each iteration of computation. The thermal path has a discrete form defined by the number of iterations, the time step that separates two successive iterations and the value of the temperature at each iteration.

The two thermo-metallurgical states are defined in two successive iterations on the thermal path:

- A previous state at t^- designated by: $E^-\left(t^-, T^-, \dot{T}^-, Z^-, Z_X^-, Z_M^-, d^-\right)$.
- A current state at t^+ designated by: $E^+\left(t^+, T^+, \dot{T}^+, Z^+, Z_X^+, Z_M^+, d^+\right)$.

X Designates one of the following phases: bainite, ferrite and perlite. $Z_X^-$and Z_X^+ are the ratio of phase X at the previous and current calculation iteration. $Z_M^-$and Z_M^+ are respectively the martensitic phase ratio at the last and current calculation iteration.

The problem is as follow: we know the initial metallurgical state at the earlier calculation iteration t^- as well as the thermal path defined by the couple (T^-, T^+) and we want to calculate the new metallurgical state (Z^+, Z_X^+, Z_M^+, d^+) at the current iteration t^+.

4.2.1. Heating stage

For the heating stage, we solve the Leblond's equation by temporal discretization according to an explicit path (Equation 21):

$$Z^+ = dt.\frac{(Z_{eq}(T^+) - Z^-(T^+))}{\tau(T^+)} + Z^- \tag{21}$$

We solve the Gray and Higgins's equation by temporal discretization according to an explicit path (Equation 22):

$$d^+ = d^- + \frac{dt}{\lambda}.\left(\frac{1}{d^-} - \frac{1}{d_{lim}}\right) - \frac{z^+ - z^-}{z}.d^- \tag{22}$$

4.2.2. Cooling Stage

For diffusive transformation, Waeckel's model provides the austenitic phase evolution (Equation 14). The function $f(t, T, \dot{T}, Z; d)$ is interpolated at each iteration of the calculation from the CCT digital diagram according to the Equation 23:

$$f(t, T, \dot{T}, Z; d) = \frac{Z_f - Z^-}{T_f - T^-}.\dot{T}^+ \tag{23}$$

The couple (t_f, T_f) is calculated by solving the intersection equation between the bearing $[E^-E^+]$ and the segment $[E_{f1}E_{f2}]$ (Figure 3). The thermo-metallurgical state at the points E_{f1} and E_{f2} is defined from CCT digital diagram (Figure 4). It is knowing the values of the metallurgical state at the edges of the interpolation segments E_{f1} and E_{f2}, the ratio Z_f is calculated by the inverse segment method (Equation 24):

$$Z_f = (Z_{f2} - Z_{f1}) \frac{t_f - t_{f1}}{t_{f2} - t_{f1}} + Z_{f1} \quad (24)$$

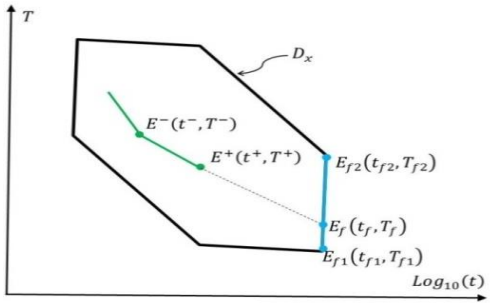

Figure 3 Interpolation of Waeckel's model

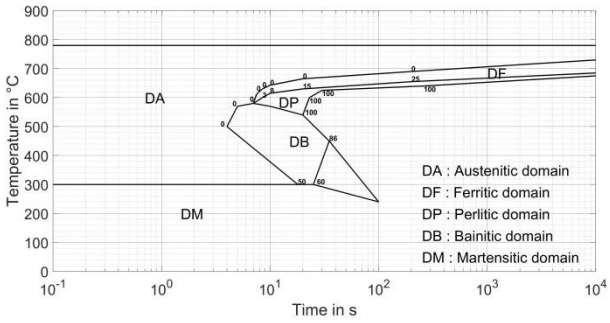

Figure 4 Numerical continuous cooling transformation diagram of C50 Steel

For martensitic transformation, the austenitic ratio is given by Equation 25:

$$Z^+ = Z_{max}.[1 - exp\,(-0.011x(Ms - T^+)] \quad (25)$$

4.3. Numerical Results

4.3.1. Test Description

The numerical calculations correspond to the realization of a fusion line carried out on a C50 steel plate by a TIG welding station. The plate is irradiated over its surface and up to half of its length. The fusion line begins 7mm from the edges of the container to eliminate edge effects. The heat source is modeled by a surface uniform heat distribution on a square of side a = 10mm and moves along the length at 0.72mm/s. The welding voltage is U = 15.2 V and the efficiency of the station is η = 0.58. The outside exchange is by convection and radiation by adopting an exchange coefficient by convection h = 5 W/m².K and a radiation emissivity ε = 0.75 where Stephan Boltzmann's constant is σ = 5,5 10^{-8} W / m².K⁴. Two values of the current intensity will be investigated: 100A and 130A. In this test, the initial metallurgical structure of the plate is a mixture of 70% of perlite and 30% of ferrite.

4.3.2. Prediction Analysis of Thermal Modeling

Figure 5 illustrates temperature distributions. The localized heat input creates a molten metal bath (T>1500°C). After the heat source move, the molten zone is cooled by conduction and convection.

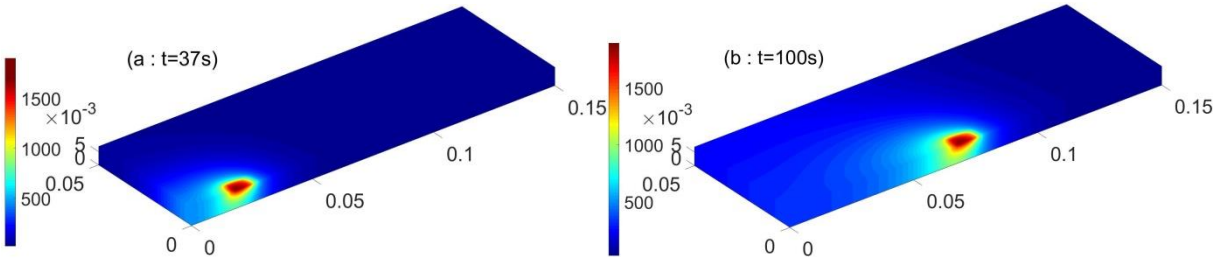

Figure 5 Temperature field for two instants of welding.

4.3.3. Prediction Analysis of the Phase Transformation

In this part we represent the prediction of the evolution of the microstructure at two point : (c_1) and (c_2) located respectively at 1 mm and at 5 mm under the welding axis and at 60 mm from the edge of the plate ($c_1(x = 60mm; z = -1mm)$ and $c_2(x = 60mm; z = -5mm)$.

Figure 6 exhibits the evolution of the metallurgical transformation for different welding conditions and at different points of the weld bead. By supplying more heat to the plate

(preheating or more intense welding current), the cooling rate decreases which promotes transformations by diffusion.

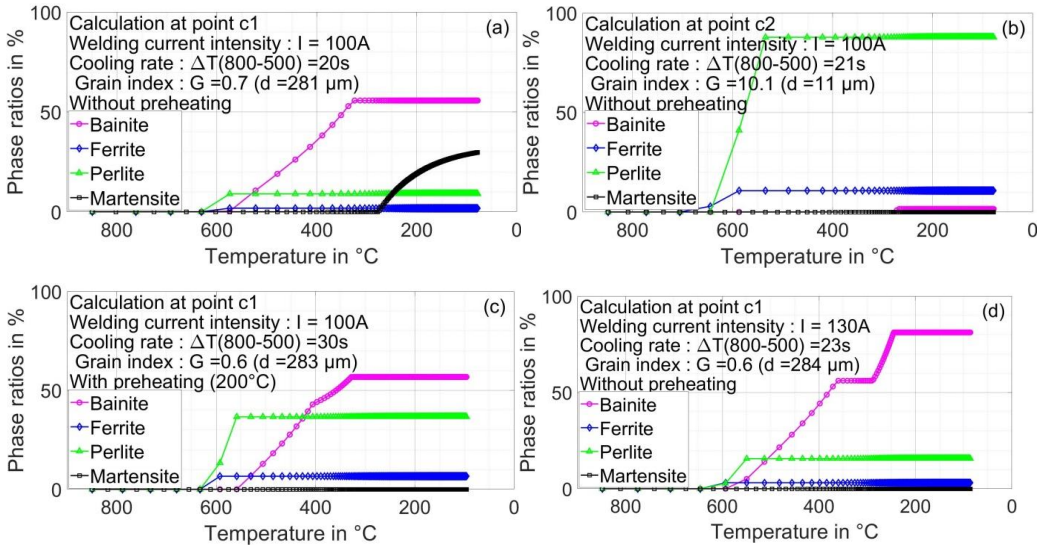

Figure 6 Evolution of the metallurgical transformation for different welding conditions and at various points of the weld bead

5. Experimental Investigation

5.1. Experimental Test

We used A TIG welding station to make a fusion line on a C50 plate. All detail for the experimental test is given in Agrebi et al. (2019).

The welded samples are cut according to the fusion line section. Small pieces of these samples are polished with abrasive paper and alumina. Then, they are attacked by a solution of 3% nitric acid and 97% alcohol. We observed the samples under an optical reflection microscope to determine the HAZ's morphology and its new metallurgical structure. We used the count and compare method to determine the evolution of the austenitic grain size in the thickness of the plate. Finally, Vickers-hardness measurements were carried out to characterize the metallurgical structure in the HAZ.

5.2. Experimental Result

Figure **7** illustrates the macroscopic observation of specimens. Immediately after the chemical attack, we note the appearance of HAZ around the melting zone. Base material in the region far from the weld pool shows almost no changes since the influence of the temperature is weak.

Figure 7 Optical macrograph cross-section of the weld bead for welding current intensity I=100 A (section at 60 mm from the edge of the plate)

Figure 8 shows the microscopic observations (magnification: 100) of specimens. Microscopic observations of the melting zone show that it is characterized by strong grain growth compared to the base material. The value of the diameter of austenitic grains

reaches 280 microns. The austenitic grain growth decreases from the fusion zone to the base material.

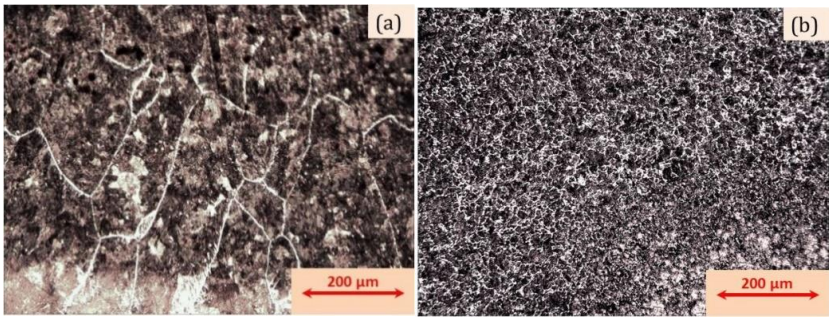

Figure 8 Microscopic observation in the thickness of the plate (magnification 100, section 60 mm from the edge of the scale, welding intensity 100A: (a) 0.5 mm below the upper surface, (b) 3.5 mm below the upper surface

6. Comparative Analysis

Figure 9 compares the HAZ observed experimentally and that simulated numerically. We notice a satisfactory agreement between the numerical and experimental results.

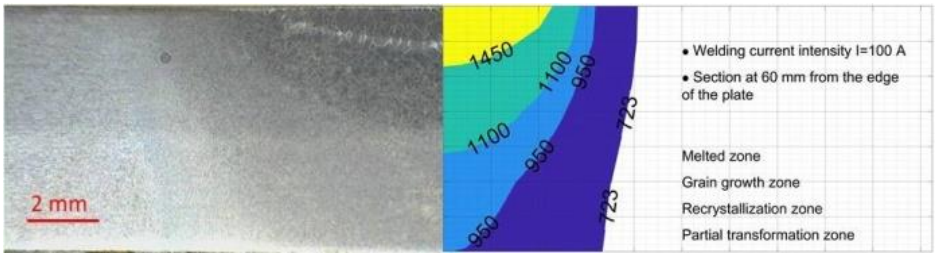

Figure 9 Comparison between optical observations and numerical predictions

Figure 10 illustrates the comparisons between the experimental measurements and the numerical calculations. Figure10.a presents the distribution in the plate thickness of the austenitic grains diameters. Figure10.b shows the evolution of the hardness according thickness. Pretty high temperatures characterize the molten zone, hence the appearance of large austenitic grains. Large grains favor a martensitic transformation (lack of grain joins for nucleation) which explains the reasonably high hardness in the molten zone.

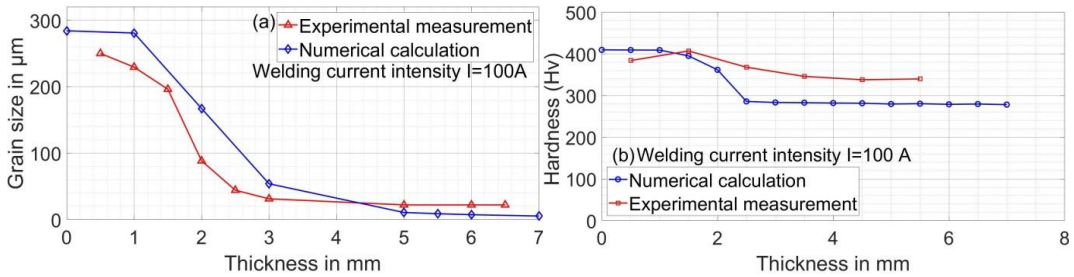

(a) (b)

Figure 10 Austenitic grain diameter (a) and hardness (b) evolution in the different zones of the HAZ (section at 60 mm from the edge of the plate)

7. Conclusions

In this study, we developed a numerical calculation code, under the environment of the MATLAB software, based on a coupled thermo-metallurgical modeling. This tool is a powerful means that can be used to optimize welding parameters. Numerical calculations show that the metallurgical transformations during a welding operation are heterogeneous.

They depend on the relative position to the heat source, the welding power and the initial temperature of the plate. In addition to the numerical study, experimental investigations are carried out to characterize the metallurgical structure obtained after the welding operations. The comparison analysis shows a good agreement between the simulated and experimental results. The developed model can predict phase transformation in the heat-affected zone after welding.

References

Agrebi, K., Belhadj, A., Bouhafs, M., 2019. Three-Dimensional Numerical Simulation of a Gas Tungsten Arc Welding Process. *International Journal of Technology*, Volume 10(4), pp. 689–699

Baskoro, A.S., Masuda, R., Suga, Y., 2011. Comparison of Particle Swarm Optimization and Genetic Algorithm for Molten Pool Detection in Fixed Aluminum Pipe Welding. *International Journal of Technology*, Volume 2(1), pp. 74–83

Baskoro, A.S., Muzakki, H., Kiswanto, G., Winarto, 2017. Effects of Micro Resistance Spot Welding Parameters on the Quality of Weld Joints on Aluminum Thin Plate AA 1100. *International Journal of Technology*, Volume 8(7), pp. 1306–1313

Deng, D., 2009. FEM Prediction of Welding Residual Stress and Distortion in Carbon Steel Considering Phase Transformation Effects. *Materials and Design*, Volume 30(2), p. 359–366

Hamide, M., Massoni, E., Bellet, M., 2008. Adaptive Mesh Technique for Thermal–Metallurgical Numerical Simulation of Arc Welding Processes*. International Journal for Numerical Methods in Engineering,* Volume 73 (5), pp. 624–641

Heinze, C., Schwenk, C., Rethmeier, M., 2012. Numerical Calculation of Residual Stress Development of Multi-Pass Gas Metal Arc Welding. *Journal of Constructional Steel Research,* Volume 72, pp. 12–19

Hendili, S., 2013. Modèles de Comportement Métallurgique des Aciers *(Metallurgical Behavior Models Steels)*, Code Aster, Clé : R4.04.01, pp. 1–28

Li, S., Ren, S., Zhang, Y., Deng, D., Murakawa, H., 2017. Numerical Investigation of Formation Mechanism of Welding Residual Stress in P92 Steel Multi-Pass Joints. *Journal of Materials Processing Technology*, Volume 244, pp 240–252

Ronda, J., Oliver, G.J., 2000. Consistent Thermo-Mechano-Metallurgical Model of Welded Steel with Unified Approach to Derivation of Phase Evolution Laws and Transformation-Induced Plasticity. *Computer Methods in Applied Mechanics and Engineering,* Volume 189(2), pp. 361–418

Rupajati, P., Clarissa, K.G., Baskoro, A.S., Kiswanto, G., Winarto, 2021. Characteristics of Mechanical Properties and Microstructure of Micro Friction Stir Spot Welding of AA1100 and Brass. *International Journal of Technology,* Volume 12(6), pp. 1302–1311

Sun, J., Hensel, J., Klassen, J., Nitschke-Pagel, T., Dilger, K., 2019. Solid-State Phase Transformation and Strain Hardening on the Residual Stresses in S355 Steel Weldments. *Journal of Materials Processing Technology,* Volume 265, pp. 173–184

Xia, J., Jin, H., 2018. Numerical Modeling of Coupling Thermal–Metallurgical Transformation Phenomena of Structural Steel in the Welding Process. *Advances in Engineering Software*, Volume 115, pp. 66–74

Zain-Ul-Abdein, M., Nélias, D., Jullien, J-F., Boitout, F., Dischert, L., Noe, X., 2011. Finite Element Analysis of Metallurgical Phase Transformations in AA 6056-T4 and Their Effects Upon the Residual Stress and Distortion States of a Laser Welded T-joint. *International Journal of Pressure Vessels and Piping,* Volume 88(1), pp. 45–56